Carbon Nanotube Degradation in Macrophages: Live Nanoscale Monitoring and Understanding of Biological Pathway

Dan Elgrabli,[†,#] Walid Dachraoui,[‡,#] Cécilia Ménard-Moyon,[§] Xiao Jie Liu,[∥] Dominique Bégin,[∥] Sylvie Bégin-Colin,[⊥] Alberto Bianco,[§] Florence Gazeau,[*,†] and Damien Alloyeau[*,‡]

[†]Laboratoire Matière et Systèmes Complexes, UMR7057 CNRS/Université Paris Diderot, Paris 75205, France, [‡]Laboratoire Matériaux et Phénomènes Quantiques, UMR7057 CNRS/Université Paris Diderot, Paris 75205, France, [§]CNRS, Institut de Biologie Moléculaire et Cellulaire, Laboratoire d'Immunopathologie et Chimie Thérapeutique, 67000 Strasbourg, France, [∥]Institut de Chimie et des Procédés pour L'Energie, l'Environnement et la Santé (ICPEES) UMR 7515, Université de Strasbourg, 25 rue Becquerel, 67087 Cedex 2 Strasbourg, France, and [⊥]Institut de Physique et Chimie de Strasbourg (IPCMS), UMR 7504 CNRS-Université de Strasbourg, 23 rue du Loess, BP 34, 67034 Cedex 2 Strasbourg, France. [#]These authors contributed equally.

ABSTRACT Despite numerous applications, the cellular-clearance mechanism of multiwalled carbon nanotubes (MWCNTs) has not been clearly established yet. Previous *in vitro* studies showed the ability of oxidative enzymes to induce nanotube degradation. Interestingly, these enzymes have the common capacity to produce reactive oxygen species (ROS). Here, we combined material and life science approaches for revealing an intracellular way taken by macrophages to degrade carbon nanotubes. We report the *in situ* monitoring of ROS-mediated MWCNT degradation by liquid-cell transmission electron microscopy. Two degradation mechanisms induced by hydroxyl radicals were extracted from these unseen dynamic nanoscale investigations: a non-site-specific thinning process of the walls and a site-specific transversal drilling process on pre-existing defects of nanotubes. Remarkably, similar ROS-induced structural injuries were observed on MWCNTs after aging into macrophages from 1 to 7 days. Beside unraveling oxidative transformations of MWCNT structure, we elucidated an important, albeit not exclusive, biological pathway for MWCNT degradation in macrophages, involving NOX_2 complex activation, superoxide production, and hydroxyl radical attack, which highlights the critical role of oxidative stress in cellular processing of MWCNTs.

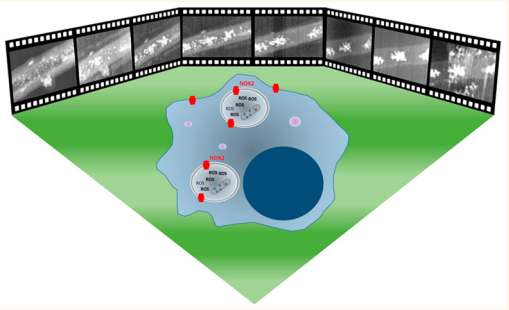

KEYWORDS: biodegradation · carbon nanotubes · macrophages · genetic response · liquid-cell transmission electron microscopy · reactive oxygen species

Although carbon nanotubes (CNTs) are one of the most promising nanomaterials for technological and pharmaceutical applications,[1,2] many gray areas remain on their life cycle in biological environments, notably regarding their biodegradation mechanisms that drastically impact their efficiency and innocuousness. In the last years, a few studies have investigated CNT biokinetics (translocation, biodistribution and clearance) *in vivo*,[3−5] revealing that, like most nanomaterials, their "journey" in the organism mainly ends in macrophage cells in lung after intratracheal instillation,[3,6] or in liver and spleen after intravenous injection.[7,8] A slow degradation of CNTs seems to occur in phagosomes,[3,9] but the biochemical and structural processes involved in the degradation of graphitic nanostructures remain unclear. *In vitro* enzymatic biodegradation of CNTs have shown that horseradish peroxidase (HRP), an enzyme from plant, can oxidize single-walled CNTs (SWCNTs) in the presence of low levels of hydrogen peroxide.[10] CNT biodegradation studies were then extended to other peroxidases such as myeloperoxidase (MPO)[11] present in neutrophils, eosinophil peroxidase (EPO),[12] and lactoperoxidase (LPO)[13] expressed by goblet cells found in the epithelial lining of the respiratory tract as well as in many human exocrine

* Address correspondence to damien.alloyeau@univ-paris-diderot.fr, florence.gazeau@univ-paris-diderot.fr.

Received for review June 18, 2015 and accepted September 2, 2015.

Published online September 02, 2015
10.1021/acsnano.5b03708

secretions. The degradation mechanisms rely on the ability of MPO, EPO, and LPO to convert hydrogen peroxide (H_2O_2) into hypochlorous, hypobromous, and hypothiocyanous acids, respectively. As observed for microorganisms, SWCNTs can be entrapped by a network of chromatin and proteins outside the cells and undergo acellular MPO-mediated biodegradation.[14] In the same way, nonenzymatic degradation medium constituted by phagolysosome elements associated with H_2O_2 is also able to degrade CNTs.[15] All these results emphasize the capacity of oxidant species to induce CNT degradation. Kagan and co-workers have recently demonstrated the ability of lung macrophages to degrade CNTs in extracellular fluid using superoxide/peroxynitrite oxidative pathways.[16] Here, we combined materials sciences and biological approaches to reveal another way taken by macrophages to degrade functionalized multiwalled carbon nanotubes (MWCNTs) in intracellular compartments, which also involves the oxidizing power of reactive oxygen species (ROS) produced by an enzymatic complex. On the one hand, *in situ* transmission electron microscopy (TEM) in liquid provided an unprecedented live monitoring of the ROS-induced damages in MWCNT structure. On the other hand, molecular and chemical biology highlighted the crucial role of NADPH oxidase 2 (NOX_2) enzymatic complexes in the ROS-production mechanisms responsible for MWCNT degradation.

RESULTS AND DISCUSSION

Structural Degradation of MWCNTs Induced by ROS in Macrophages. We carried out TEM analyses of the structural degradation of MWCNTs as a function of their aging time (t_{ag}) in THP-1 cells differentiated into macrophages. These studies were performed with two types of nanomaterials: MWCNTs and MWCNTs filled with magnetic iron oxide nanoparticles (namely, Fe@MWCNTs). These latter were synthesized with a high-yield two-step process.[17] In both cases, MWCNTs were functionalized by arylation to introduce amino groups on the nanotube sidewall and to ensure a good dispersion in physiological media. In view of cytotoxicity assessments after 24 h exposure to CNTs (Figure S1), we choose a dose of MWCNTs and Fe@MWCNTs of 5 μg/mL inducing a cell-death degree below 5%. After t_{ag} of 3, 24, 48, and 168 h, CNTs were extracted from cells to perform TEM observations. As can be seen in Figure 1a for MWCNTs and Figure S2 for Fe@MWCNTs, the graphitic nanostructures are deeply scarred by cells. The main stigmata of degradation processes are the presence of holes in the carbon walls. High resolution TEM allows confirming that these holes can be either drilled through one side or through the whole nanotube structure (Figure S3a–c). The t_{ag}-dependent analyses of the percentage of perforated area (P_a, Figure 1b), the average surface area of holes ($\bar{S}$, Figure 1c), and the number of holes per surface unit (D, Figure 1d) provide a better overview of the degradation mechanisms. The degradation of MWCNTs quickly increases over time in cells, with P_a reaching 51% after 168 h aging. However, the 25-fold increase of P_a when increasing t_{ag} from 3 to 168 h is concomitantly due to the increments of $\bar{S}$ and D that vary as $t^{1/3}$ and $t^{1/2}$, respectively. As $P_a = \bar{S} \times D$, our measurements allow the evaluation of the respective weight of the nucleation and growth of holes on the expansion of structural damage in MWCNTs. The fast increase of D, yet slowed down by the coalescence of holes, reveals that MWCNTs present many energetically affordable onset of degradation and indicates that the degradation mechanisms are not dominated by the expansion of holes drilled on sparse preferential sites. We also noted that the mean thickness of the nanotube walls was reduced by 15% after 168 h in macrophages. Figure 1e shows that the amount of ROS quantified by 2′,7′-dichlorodihydrofluorescein diacetate (DCFDA) is approximatively 3-fold increased when MWCNTs or Fe@MWCNTs are incubated 24 h with THP-1-derived macrophages. This enhanced production of ROS is in agreement with previous studies on other macrophages,[18] and it highlights the possible role of these highly oxidative species in the degradation of exogenous nanomaterials.[11,19,20] To test this hypothesis, we assessed the effects of *N*-acetyl-L-cysteine (NAC), a ROS scavenger inducer, on degradation of MWCNTs. NAC significantly reduced the cellular production of ROS, which was still 20% higher than the untreated control (Figure 1e). Interestingly, the presence of NAC substantially prevented the degradation of both MWCNTs and Fe@MWCNTs. Up to 3-fold decrease of P_a was measured after 48 h of intracellular aging in the presence of NAC, while both $\bar{S}$ and D were also reduced (Figure 1b–d). This confirms that antioxidant inducers diminish both nucleation and growth of cell-induced damages in MWCNTs. The kinetics and mechanisms of degradation of Fe@MWCNTs are very similar to the ones of MWCNTs, suggesting that iron embedded into nanotubes do not interplay with the degradation mechanisms. The relevance of all these statistical measurements was validated by Kolmogorov–Smirnov tests (Figure S4).

As these important alterations of the graphitic structures could also modify the cytotoxicity effects of CNTs over time, we evaluated if the products of degradation extracted from cells 24 h after exposure are more or less toxic than the original forms. Using Alamar blue assay, we compared the lethal dose inducing 50% cell death (LD_{50}) for MWCNTs, Fe@MWCNTs, and their degradation products (namely, dMWCNTs and dFe@MWCNTs, respectively). Interestingly, Figure S5 shows that the degradation products are less toxic (LD_{50} was 47.2 and 54.3 μg/mL for dMWCNTs and dFe@MWCNTs, respectively) than the original nanosystems (LD_{50} was 27.7 μg/mL for both MWCNTs

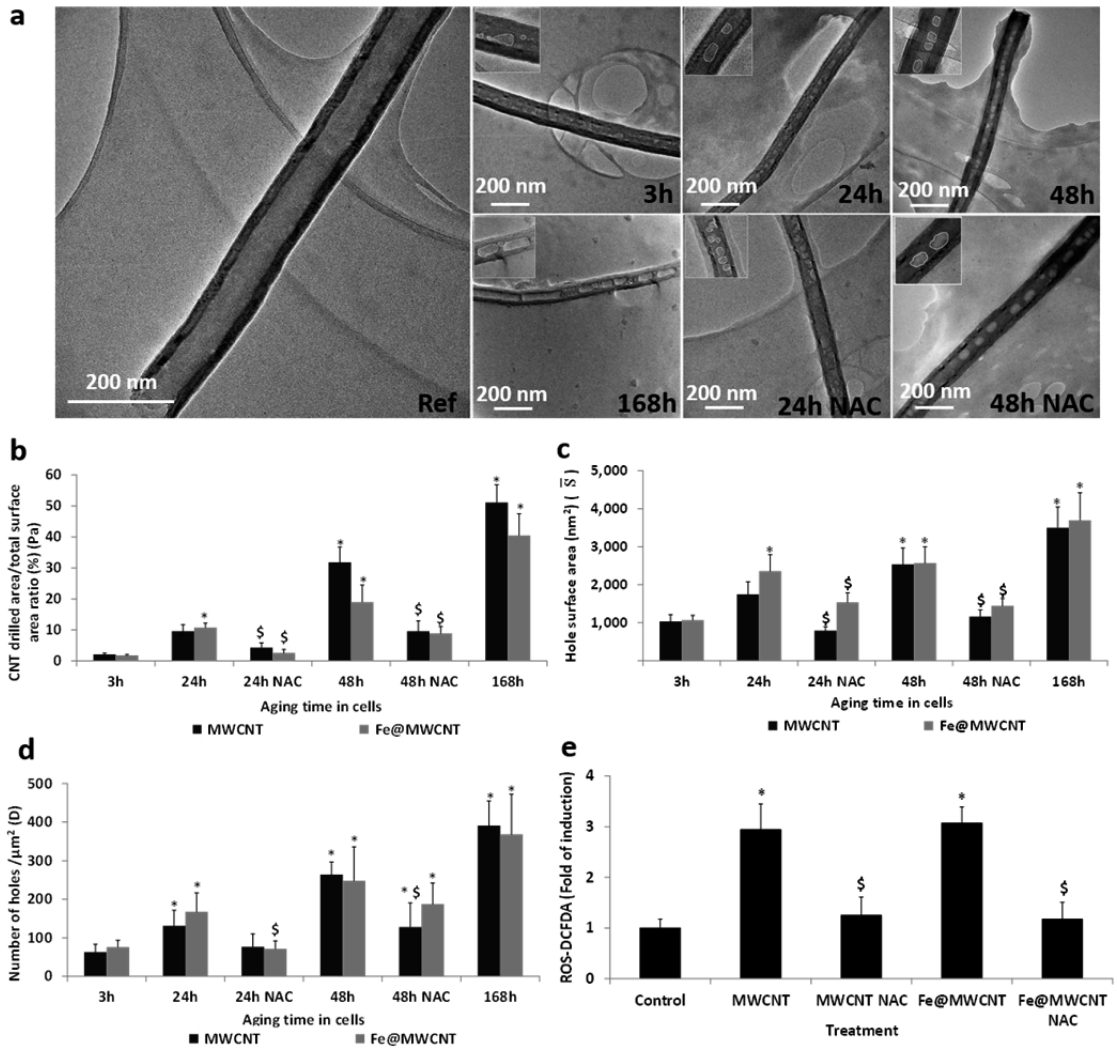

Figure 1. MWCNT and Fe@MWCNT degradation in THP-1 differentiated into macrophages. (a) TEM observations of MWCNTs before (ref) and after aging into cells. The aging time and the presence of NAC in cells are indicated in the bottom right corner of each image. (b) Ratio of total perforated area to total surface area (P_a), (c) mean surface area of holes ($\bar{S}$), and (d) density of holes (D) in MWCNTs or Fe@MWCNTs as a function of the aging time in cells and the presence or absence of NAC. (e) Formation of ROS in THP-1 after treatment with a 5 μg/mL suspension of MWCNTs or Fe@MWCNTs for 24 h. ROS were detected by fluorescence measurement of the DCFDA reporter and results are given in fold of untreated controls. Data shown in panels b−d are from three independent experiments (minimum 50 observed items) and are expressed as mean values ± SD. Results in panel e are the mean ± SD of 3 separate experiments, each carried in triplicates. Asterisk (*) designates a statistically significant difference from 3 h group ($p < 0.05$) (panels b−d) or control group (panel e). Dollar symbol ($) designates a statistically significant difference between MWCNT NAC or Fe@MWCNT NAC groups and its respective equivalent MWCNT or Fe@MWCNT group without NAC treatment ($p < 0.05$).

and Fe@MWCNTs), revealing that cell processing of MWCNTs tends to minimize their cytotoxicity.

Reducing the gap between *in vitro* and *in vivo* investigations is an essential prerequisite to fully understand CNT lifecycle in the organism and to exploit this knowledge in biomedicine. As a first step, we compared the degradations of graphitic structures in cell cultures and in animals. Rats were exposed to MWCNTs *via* intratracheal instillation and *ex vivo* TEM analyses revealed the presence of exogenous nanomaterials in macrophages of the lungs and the lymph nodes, 7 days after the exposure (Figure S6). However, by analyzing closely these TEM experiments, we can clearly observed the presence of many holes in the structure of the tubes. Therefore, these highly perforated nanotubes indicate that the oxidative degradation processes analyzed over time through *in vitro* approach are very similar to the structural alterations of CNTs occurring *in vivo*.

***In Situ* Nanoscale Monitoring of the ROS-Induced Damages in MWCNTs.** Liquid-cell TEM has provided the opportunity to follow nanoscale processes at the interfaces between liquids and solids, opening many avenues in both material and life sciences.[21,22] It is well-established that the electron-beam irradiation of water generates the following primary products by radiolysis: hydrated electrons (e_h^-), hydrogen radicals ($H^\bullet$), hydroxyl radicals ($OH^\bullet$), dihydrogen (H_2), H_2O_2, hydronium ions

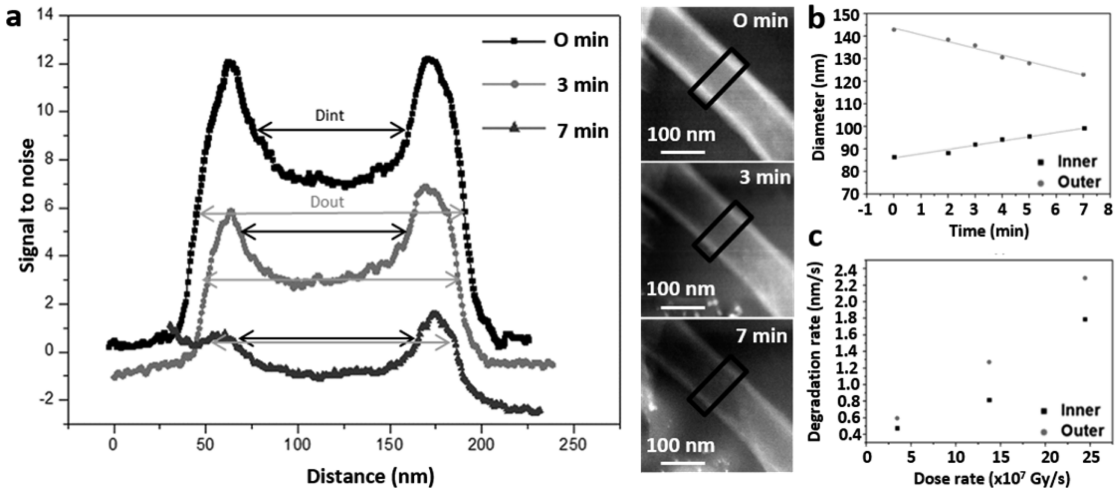

Figure 2. *In situ* **liquid TEM in water. Dose-dependent thinning of MWCNTs due to OH• produced by radiolysis. (a) Time evolution of signal-to-noise ratio (SNR) profile measured across a MWCNT, during non-site-specific degradation. The position and the width (100 nm) of the SNR profiles are indicated on the three STEM-HAADF images acquired at 400K magnification (corresponding dose rate of 2.4 × 10^8 Gy·s^{-1}, see Methods) after 0, 3, and 7 min of irradiation. The inner (D_{int}) and outer (D_{out}) diameters were measured by considering the position of the sidewalls as the half-maximum of the corresponding peaks on the SNR profiles. (b) Time evolution of the inner and outer diameters of the MWCNT degraded in (a). The concomitant increase of the inner diameter and decrease of the outer diameter reveal that degradation occurs inside and outside of the MWCNTs. Linear regressions were applied to the size evolution of inner and outer diameters as a function of time, from which the slope corresponds to their kinetic of degradation. (c) Degradation rate (nm/s) of the inner and outer diameters of CNT as a function of the electron dose given in Gy·s^{-1} (see Methods).**

(H_3O^+), and hydroperoxyl radicals ($HO_2^•$).[23] When nanoscale analyses are performed in water, these species are uniformly distributed within the irradiated region with concentrations varying as sublinear power laws of the electron-dose rate ($\dot{d}$).[24] The straightforward control over the local production of strong reducing agent (e_h^-, H•) has been deeply exploited to study the nucleation and growth of metal nanoparticles *via* the reduction of metallic precursor.[25−29] Here, we investigated the degradation mechanisms of MWCNTs and Fe@MWCNTs in water under electron beam irradiation and we identified the oxidizing species involved in this chemical attack. Structural modifications of MWCNTs were simultaneously generated and imaged in scanning transmission electron microscopy (STEM) mode at 80 kV. Signals were collected with a high annular angular dark field (HAADF) detector. The high signal-to-noise ratio of STEM-HAADF imaging, in which $\dot{d}$ is proportional to the square of the magnification, allows us to distinguish two mechanisms in the degradation of MWCNTs. Figure 2a illustrates that the cylindrical nanostructures sustain a wall-by-wall thinning until breaking of the tube. Interestingly, this erosion occurs all along the irradiated surfaces of CNTs. Intensity profiles measured perpendicularly to the anisotropy axis also reveals that both inner and outer sides of the MWCNTs are attacked, suggesting that chemical species are also generated inside the inner cavity when the electron beam passes through the nanotubes. This induces a reduction of the outer diameter and an increase of the inner diameter that were measured to be linear with time (Figure 2b). By defining the speed of thinning process as the slope of the linear relation of diameters and time, we demonstrated that the kinetics of degradation is enhanced with $\dot{d}$. For example, the speed of degradation for the outer diameter was boosted from 0.6 to 2.3 nm/s, when stepping up $\dot{d}$ from 3.4 × 10^7 Gy·s^{-1} (magnification of 150K) to 2.4 × 10^8 Gy·s^{-1} (magnification of 400K) (Figure 2c). Together with this non-site-specific thinning, MWCNTs sometimes endure more severe damages consisting in transversal drillings of the walls. Figure 3a shows that this second degradation mechanism can either generate spherical holes if the drilling axis is almost perpendicular to the tube axis or can tear the nanotubes lengthwise for more grazing drilling angles, pulling out together many walls from the tubes and creating elongated holes. As these drilling processes were not systematically observed, one can reasonably assume that pre-existing defects in the MWCNTs (pentagon-hexagon pairs, atomic vacancies, dislocations, presence of functional groups that lead to the formation of sp^3 hybridized carbon atoms, *etc.*), which are more reactive due to deformation, may favor this faster degradation mechanisms. This assumption is strengthened by the degradation mechanisms of Fe@MWCNTs that in rare cases present iron oxide nanoparticles inserted in between the nanotubes walls (Figure 3b). As observed by *ex situ* HRTEM (Figure S7), the MWCNT structure presents a high rate of crystalline defects in these interface areas. These highly reactive zones systematically serve as onset for transversal drilling by tearing along the interface between the tube and the nanoparticles. Figure 3b (100 and 120 min of

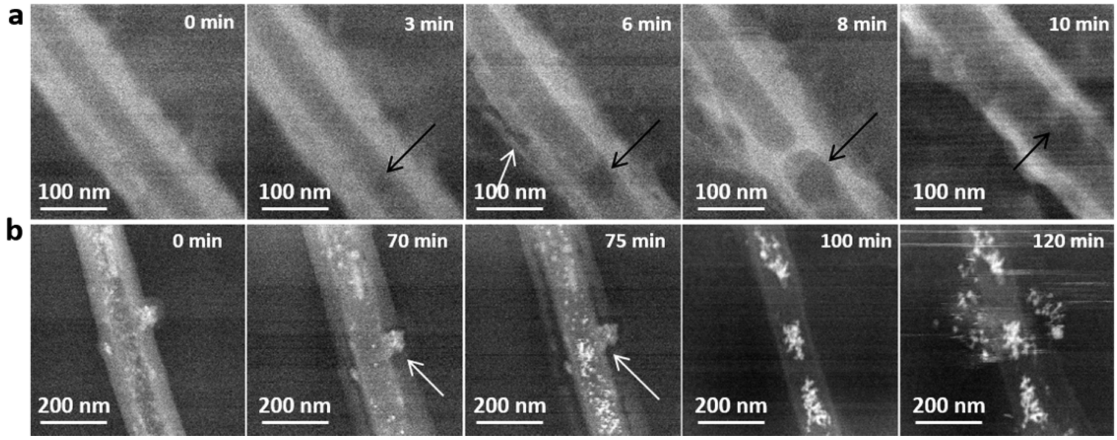

Figure 3. *In situ* **liquid TEM in water. Site-specific drilling of MWCNTs induced by OH• chemical attack. Time series of STEM-HAADF images with the observation time indicated in the top right corner of each image. (a) Drilling process in a MWCNT acquired with a magnification of 400K (corresponding dose rate of 2.4 10^8 Gy·s^{-1}, see Methods). Black arrows indicate the nucleation and growth of a spherical hole and the white arrow shows a tearing of the nanotube along the anisotropy axis. A video file of this image series accelerated 16 times can be seen in Supporting Information. (b) Drilling process in a Fe@MWCNT acquired with a magnification of 200K (corresponding dose rate of 6 $\times$ 10^7 Gy·s^{-1}, see Method). White arrows show a tearing of the nanotube along the interface between the graphitic structure and the iron oxide nanoparticles inserted in the carbon walls.**

observation) also illustrates that the degradation of the last remaining walls of nanotubes frequently occurs through a slower wall-by-wall thinning. Although the encapsulated iron oxide nanoparticles move inside the MWCNTs under beam irradiation, their dispersion in the liquid cell is possible only after the rupture of the tubes, illustrating the potential of biodegradable MWCNTs for drug delivery applications.[30]

It is worth to note that no structural alteration was observed when MWCNTs and Fe@MWCNTs were irradiated for several hours with the same optical conditions under vacuum (Figure 4a). As the energy of incident electrons was below the knock-on-damage threshold in MWCNTs, the degradation processes observed in water are unambiguously induced by chemical reactions. Furthermore, both wall-by-wall thinning and drilling mechanisms were exclusively observed in the irradiated areas showing the short lifetime and very low diffusion of the involved chemical species. Schneider *et al.* have calculated that among the radiolysis products only the highly reactive species (e_h^-, H•, OH•) are strictly restricted to the irradiated region. Thus, the strong oxidation potential of OH• makes it the most likely candidate for the chemical degradation of MWCNTs. The dose-dependent concentration of this short-lived ROS, which varies as $\dot{d}^{0.46}$,[24] is also consistent with the degradation boosting observed for higher magnifications. This damaging role of OH• was definitely confirmed by the long-term stability of MWCNTs in ethanol (Figure 4b), in which ionizing radiations generate peroxyl radicals, but no OH•.[31]

Additionally, the two mechanisms of degradation extracted from these *in situ* TEM observations are in agreement with previous spectroscopy studies that suggested two concomitant destructive interactions of OH• with MWCNTs:[32] (1) OH• could preferentially attack MWCNTs at the defect sites to produce carboxylic acid groups leading to disordered and perforated walls. Note that, the covalent functionalization by arylation induces the rehybridation of sp^2 carbon atoms to sp^3, thus increasing the amount of defects and the reactivity of the MWCNTs toward OH• in the vicinity of the functionalized carbon atoms. (2) OH• could also insert a significant amount of hydroxyl groups on unsaturated C═C bonds of the nanotube sidewalls by electrophilic addition reaction, which are then converted into quinones and eventually carboxylic acids. MWCNT functionalization also imparts enhanced hydroxyl radical capture ability, in particular OH•.[33−35] Interestingly, the presence of hydroxyl and carbonyl functions was detected on MWCNTs extracted from rat lung.[3] These oxygen-containing functional groups emphasize the putative role of OH• in MWCNT degradation in cells. Although the dynamic processes observed *in situ* are much faster than those occurring in cells because of the higher concentration of ROS (around 10^{-5} M[24] *versus* less than 10^{-6} M in phagosome[36]), the two mechanisms of degradation can also explain the thinner and highly perforated walls of the tubes extracted from macrophages. The non-site-specific thinning certainly allows the exposition of subsurface defects to ROS resulting in the drilling of many holes in MWCNTs.

Biological Pathway for MWCNT Degradation by Macrophages. As both *in situ* and *in vitro* nanoscale studies suggest the crucial role of ROS in the degradation of MWCNTs, we focused on the biological pathway for the production of ROS and particularly OH•. In cells, MWCNTs are degraded into phagosomes,[3] and NOX_2 complex is well-known to be associated with the plasma and the phagosomal membranes. This enzymatic complex was described to be a biocatalyst of the reduction of

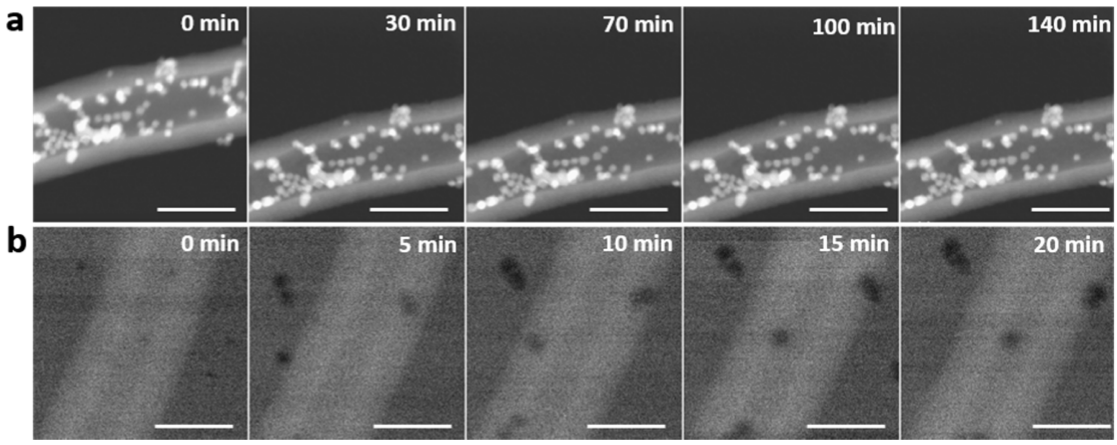

Figure 4. Stability of MWCNTs and Fe@MWCNTs under similar beam irradiation conditions in vacuum and in ethanol. STEM HAADF image series acquired at 80 kV with a magnification of 400K. The observation time on the analyzed area is indicated in the top right corner of each image. (a) No degradation of Fe@MWCNTs is observed under vacuum condition (conventional STEM observation) revealing the absence of knock-on damage induced by electron beam. (b) No degradation of MWCNTs is observed in ethanol in which the electron beam creates peroxyl groups but no $OH^{\bullet}$ (circular black contrasts are imaging artifacts). Scale bars correspond to 100 nm in each image.

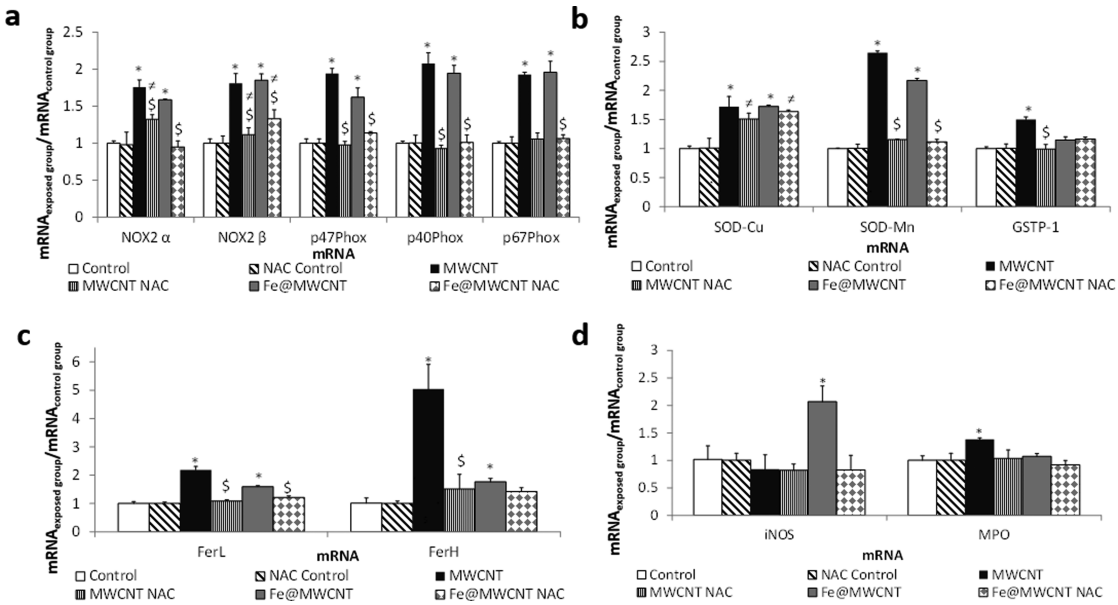

Figure 5. Effect of MWCNTs and Fe@MWCNTs on the gene expression level of NOX_2 complex and antioxidant proteins. THP-1 cells were treated with 5 μg/mL of MWCNT or Fe@MWCNT suspension. After 24 h exposure, mRNA quantification of (a) $NOX_{2\alpha}$, $NOX_{2\beta}$, p47phox, p40phox, and p67phox; (b) SOD-Cu, SOD-Mn and GSTP1; (c) Ferritin L and Ferritin H; and (d) iNOS and MPO. Results are the mean $\pm$ SD of 3 separate experiments. Asterisk (*) designates a statistically significant difference from control group ($p < 0.05$). Dollar symbol ($) designates a statistically significant difference between MWCNTs NAC or Fe@MWCNT NAC group and its, respectively, equivalent MWCNTs or Fe@MWCNTs group without NAC treatment ($p < 0.05$). Not-equal symbol ($\neq$) designates a statistically significant difference between MWCNT NAC or Fe@MWCNTs NAC and NAC control group ($p < 0.05$).

molecular oxygen to generate superoxide $O_2^{\bullet-}$ that can dismute to generate ROS species.[37] NOX-family enzymes are likely to be involved in a variety of physiological events including cell proliferation, host defense, differentiation, apoptosis, senescence, and activation of growth-related signaling pathways.[37] NOX_2 complex consists of a large association of glycoproteins named $NOX_{2\alpha}$ (or gp22phox), $NOX_{2\beta}$ (or gp91phox) and cytosolic proteins, namely p67phox, p47phox, p40phox, and Rac.[37] To assess the involvement of NOX_2 complex into the degradation processes, macrophages were exposed for 24 h to 5 μg/mL of MWCNTs or Fe@MWCNTs and total ribonucleic acid (RNA) was extracted. The mRNAs of $NOX_{2\alpha}$, $NOX_{2\beta}$, p67phox, p47phox, and p40phox were quantified by polymerase chain reaction (PCR) (Figure 5a). The mRNAs of all of these proteins were approximately induced two times as compared to the untreated cells. The protein level for $NOX_{2\beta}$ was also assessed by Western blot analysis. Both inductions at the genetic and protein levels are in

good agreement (Figure S8). Remarkably in the presence of NAC, no significant or much lower inductions were measured. Together with the nanoscale investigations of the degraded MWCNTs, the biological response of macrophages indicates a MWCNT-induced activation of NOX_2 complex and a subsequent production of ROS with the purpose of degrading exogenous nanostructures. The addition of NAC in the cellular medium inhibits the existing ROS and perturbs the retroactivity of ROS-production by NOX_2, resulting in the low activity of this complex and the lower capacity of cells to degrade MWCNTs.

When activated, NOX_2 complex is the most important source of ROS in phagocytes by $O_2^{\bullet-}$ production.[36] In the presence of superoxide dismutase (SOD), $O_2^{\bullet-}$ can dismute into H_2O_2. As described by Haber-Weiss reaction, in the presence of iron, $O_2^{\bullet-}$ and H_2O_2 produce $OH^{\bullet}$. We evaluated this possible production pathway of $OH^{\bullet}$ by quantifying SOD mRNA (Figure 5b). Cu-SOD that is preferentially located into cytoplasm was induced 1.7 times as compared to control. NAC did not change mRNA level of this protein. Mn-SOD that is preferentially located into phagosome was induced more than 2 times for MWCNTs and Fe@MWCNTs, but the presence of NAC annihilates this enhanced-mRNA level. Note that mRNA of glutathione *S*-transferase (GSTP-1), a well-known antioxidant, also increases most probably to regulate ROS production (Figure 5b). Remarkably, Fe^{3+}-catalyzed Haber-Weiss reaction[31] and its metabolism seem to play a role in the regulation of CNTs degradation *via* the production of iron storage proteins, such as ferritin. Indeed, both light chain (FerL) and heavy chain (FerH) of ferritin mRNA were induced by MWCNT and Fe@MWCNT exposure (Figure 5c), as well as the protein level for FerH (Figure S8). Nevertheless, FerH mRNA was much less increased with Fe@MWCNTs than with MWCNTs. This phenomenon indicates that the regulation of Fe^{3+} involved in the production of $OH^{\bullet}$ is influenced by the presence of magnetite nanoparticles (composed of both Fe^{2+} and Fe^{3+} ions) inside the nanotubes. With iron-free nanotubes, the cells need to provide more Fe^{3+} ions and then produce more ferritin. With Fe@MWCNTs, the cells reduce the endogenous production of Fe^{3+} ions, because of the exogenous Fe^{3+}/Fe^{2+} pool inside the tubes. These perturbations in the iron-production mechanisms employed by macrophages to degrade carbon nanotubes could generate different production rate of $OH^{\bullet}$ and could then be responsible for the slightly different degradation kinetics of MWCNTs and Fe@MWCNTs. For example, after 168 h of incubation, only 40.5% of total surface area for Fe@MWCNTs *versus* 51.1% for MWCNTs was degraded (Figure 1b).

As iNOS and MPO proteins were described to take part in CNTs biodegradation,[10,16] their roles were also investigated. Peroxynitrite-induced CNTs degradation was reported to play a significant, but not exclusive,

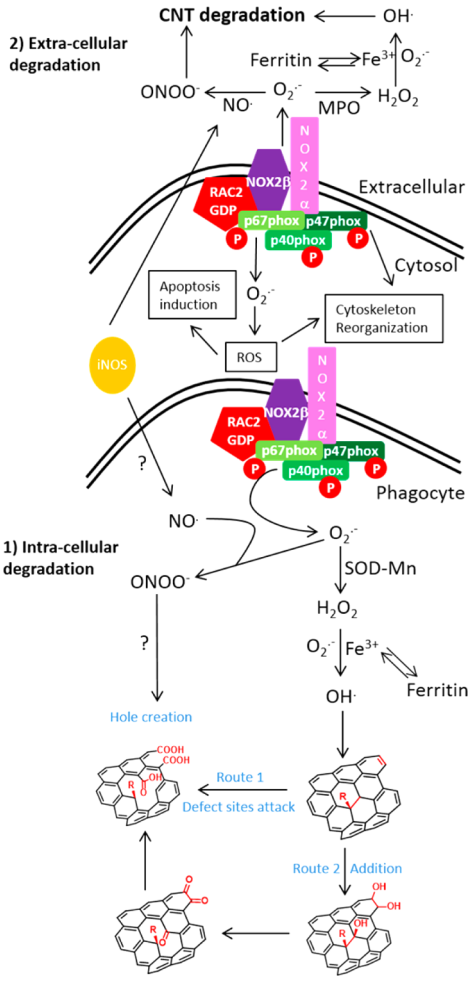

Figure 6. Schematic representation of the biological pathways of MWCNT degradation in macrophages. (1) Intracellular oxidative degradation: after engulfment of MWCNTs, NOX_2 complex is activated on cytosolic and phagosomal membranes. Active NOX_2 complex induced $O_2^{\bullet-}$ production and then cytoskeleton reorganization. Into phagosome, $O_2^{\bullet-}$ is turned into H_2O_2 by SOD and H_2O_2 is turned in the presence of Fe^{3+} into $OH^{\bullet}$ (Haber-Weiss reaction). $OH^{\bullet}$ could attack MWCNT defects and unsaturated carbon bonds on the sidewalls of CNTs to generate carboxylic acids creating holes in the graphitic structure. (2) Extracellular oxidative degradation: MWCNT outside the cells can also be degraded by two routes: (i) production of $OH^{\bullet}$ *via* NOX_2 complex and MPO, or (ii) peroxynitrite attack as described by Kagan *et al.*[16]

role in the biodegradation process.[16] Peroxynitrite production in cells is due to a nonenzymatic reaction of superoxide radicals and $NO^{\bullet}$.[38,39] In presence of MWCNT and Fe@MWCNT, iNOS mRNA was quantified as $NO^{\bullet}$ producer in cells. Interestingly, iNOS mRNA was only increased in the presence of Fe@MWCNT (Figure 5d) suggesting the ability of peroxynitrite to preferentially attack structural defect site constituted by the presence of iron. As MPO was described to take part in CNT degradation,[11] its mRNA expression was also quantified. Total mRNA for MPO was increased by 38% in treated cells compared to the control (Figure 5d), suggesting a possible implication of this protein in CNT degradation. Nevertheless, studies on

ROS produced by MPO in response to bacterial attack are mainly found in the extracellular matrix[36] indicating that MPO could be produced by cells to induce extracellular CNT degradation.

As sketched in Figure 6, macrophages employed several oxidative mechanisms to degrade CNTs outside and inside the cells. Particularly, our pluridisciplinary approach of MWCNT biodegradation in macrophages sheds light on a multistep process based on the phagocytosis of MWCNTs, the activation of NOX_2 complex into phagosomes with the purpose of producing ROS, leading to the chemical attack of the graphitic nanostructures by $OH^{\bullet}$. Furthermore, the implication of NOX_2 in the cell response to CNT allows highlighting many *in vitro* and *in vivo* studies on CNTs. NOX_2 complex needs to be associated with Rac_2 protein for its activation. Rho-GDP dissociation inhibitor (Rho GDI) is a small protein associated with Rac_2-GDP in the cytoplasm.[37] To be activated and move from the cytoplasm to the membrane, Rac_2 changes his GDP to GTP. This modification leads to the dissociation of Rac_2 and Rho GDI explaining the induction of Rho GDI protein alone in cells. Hence, the activation of NOX_2 complex demonstrated in this study could explain previous proteomic studies showing CNT-induced overactivity of Rho GDI.[40−42] Moreover, it was also established that CNTs could cause cytoskeleton protein variations in macrophages,[41,43] alveolar basal epithelial cells[40] or keratinocytes.[42] Notably, Ju *et al.* demonstrated that MWCNTs increase the actin expression in A549 cells, but this effect is significantly attenuated by the inhibition of ROS by NAC.[40] These results are in line with the NAC-induced low activity of NOX_2 complex, because p47phox has the ability to influence cytoskeletal organization.[44] Our results are also supported by an *in vivo* study on knockout mice that cannot produce $NOX_{2\beta}$.[45] After a single instillation of 40 μg of SWCNTs in the lung, alveolar macrophages and neutrophils were found in larger numbers in the bronchoalveolar fluid of knockout mice compared to normal mice. This cell accumulation was associated with production of pro-inflammatory cytokines (IL6, MCP-1, TNF) and suppression of the anti-inflammatory/pro-fibrotic response (TGFβ) that are ordinarily induced by CNTs in mice that cannot clear them.[46−48] In light of the present study, we could conclude that in the absence of $NOX_{2\beta}$, CNTs could not be degraded and pro-inflammatory response was activated. In another study, Shvedova *et al.* have shown that vitamin E deficiency enhances pulmonary inflammatory response and oxidative stress induced by SWCNTs in mice.[49] Interestingly, a study performed on HIV-gp120 protein revealed the ability of vitamin E to regulate ROS generated by NOX_2 complex, supporting the role of NOX_2 complex in the degradation of CNTs and the role of pro-inflammatory cytokine as regulator of cell response to CNTs.

CONCLUSION

The biodegradation of MWCNTs in macrophages was investigated by simultaneously examining the influences of intracellular environment on the atomic structure of nanomaterials and probing the genetic responses of the cells to CNTs. Liquid-cell TEM was exploited for the first time to follow the dynamical chemical attack of MWCNTs by $OH^{\bullet}$ at the nanoscale, revealing two electron dose-dependent routes of degradation: fast tearing and perforation of the walls are enabled on reactive structural defects, while a continuous thinning of the walls occurs in a non-site-specific manner. These nanoscale observations provide a mechanistic understanding of the ROS-induced transformations of MWCNTs that could be exploited for drug delivery applications and for better controlling the life-cycle of CNTs in biological environments. The crucial role of NOX_2 complex in the biological pathway leading to a controlled production of ROS in the vicinity of MWCNTs and their subsequent degradation was clearly established. These intracellular transformations, together with the already revealed extracellular degradation of CNTs,[16] emphasize the various oxidative mechanisms deployed by macrophages to process graphitic nanostructures. More generally, this interdisciplinary approach to study the reciprocal interactions between endogenous and exogenous species should be applied to other nanosystems and biological environments, because it provides crucial information for the development of efficient and safe nanomedicine.

METHODS

Synthesis of MWCNTs and Fe@MWCNTs. MWCNTs were provided by Pyrograph Products (Cedarville, OH). Their inner diameter varies from 40 to 80 nm. As reported in previous study,[17] to produce Fe@MWCNTs, MWCNTs were first washed with HNO_3 to remove traces of the residual iron growth catalyst. To remove the maximum number of oxygenated species on their surface, they were heated at 900 °C under an inert atmosphere for 4 h. The elimination of oxygenated groups at the surface of MWCNTs was confirmed by X-ray photoelectron spectroscopy.[50] MWCNTs were first dispersed in octadecene under ultrasonication. Iron stearate was then added, and the solution was heated at 120 °C for 12 h to dissolve the reactants, eliminate the traces of water or impurities, and favor the diffusion of metal precursors inside MWCNTs. Then, the mixtures were heated at 318 °C (heating rate 5 °C/min) under air for 2 h. Finally, the products were washed four times with ethanol and chloroform, then centrifuged, followed by a conventional filtration method to remove NPs formed outside MWCNTs.[51] After this first filling step, once the mixture was heated and cooled to room temperature, the same synthesis was repeated again without washing steps by adding iron stearate as a precursor.

Functionalization of MWCNTs and Fe@MWCNTs. MWCNTs and Fe@MWCNTs were functionalized by arylation to introduce amino groups on their sidewall and increase their dispersibility

in water.[17] Iron Mass Fraction was quantified in previous study[17] by ICP-AES revealing the absence of iron for MWCNT and an iron mass fraction of 6.64% for Fe@MWCNT.

Preparation and Characterization of MWCNT and Fe@MWCNT Suspensions. Nanotubes were suspended in cell culture media at a concentration of 100 μg/mL. The suspensions were sonicated for 5 min (5 s pause every 30 s) at 60 W with an ultrasonic bath (sonorex digitec, Bandelin). The quality of the suspensions was visually estimated and agglomerates sizes were quantified using nanoparticle tracking analysis system (Nanosight, Malvern). Agglomerate mean size was quantified to be 114 $\pm$ 1.6 and 123.7 $\pm$ 1.5 nm for MWCNT and Fe@MWCNT, respectively. Ninety percent of the agglomerates were smaller than 173 $\pm$ 2.8 and 194.7 $\pm$ 12.7 nm for MWCNT and Fe@MWCNT, respectively.

MWCNT for *in Vivo* Experiments. $MWCNT_{vi}$ (product number: 636649) was purchased from Sigma-Aldrich (Lyon, France). These nanotubes were synthesized by Chemical Vapor Deposition method. Their diameter ranged from 20 to 50 nm and their length from 0.5 to 2 μm (data from the supplier).

Cells and Cytotoxicity Test. The human monocytic cell line THP-1 was obtained from ATCC (France) and cultured in fresh supplemented media (RPMI 1640 medium supplemented with 10% FCS (Gibco, France), 2 mM glutamine (Gibco, France), 100 U/mL penicillin, and 100 mg/mL streptomycin (Gibco, France)) at 37 °C and 5% CO_2. The THP-1 cells were maintained between 10^5 and 10^6 cells/mL in fresh supplemented RPMI media. In the exponential phase of growth, cells were seeded onto 96-well plates at 80 000 cells per well. After 48 h phorbol myristate acetate (PMA) treatment at 5 ng/mL, the cells were washed and exposed for 24 h to various concentrations of MWCNTs or Fe@MWCNTs (0, 0.53, 1.06, 3.12, 6.25, 12.5, 25, 50, 75, 100 μg/mL) in RPMI media. All the suspensions were prepared extemporary in tubes and 100 μL was added directly on the cells. The cell viability was determined 24 h after treatment by Alamar blue assay (Alamar blue reagent, Biosource, France). At the end of the tests, optical density was measured on 80 μL supernatant transferred into another clean culture plate.

Oxidative Stress Assessment. Cells were seeded onto 96-well plates at 80 000 cells per well in the presence of 5 ng/mL of PMA. After 48 h, cells were washed and fresh supplemented media was added for 24 h. Then, cells were pretreated or not for 30 min with 10 mM of NAC and exposed to 5 μg/mL of MWCNTs or Fe@MWCNTs in the presence or absence of NAC. After 24 h, cells were washed with PBS, loaded with 50 μM of 2,7-dichlorofluorescein diacetate (DCF-DA) for 40 min and washed again with PBS. After a further incubation in PBS for 1 h, the fluorescence intensities were measured at 488 nm excitation and 530 nm emission in the fluorescence plate reader (Fluostar Galaxy CTC 435,BMG).

Animals. Male Sprague–Dawley rats weighing 180–220 g were purchased from Charles River Laboratories (St Germain-sur-l'Arbresle, France). The rats were kept in a conventional animal facility and had access *ad libitum* to food and drink. The experimental protocol has been approved by the local ethical committee for animal research.

TEM Experiments. All the *in situ* and *in vitro* TEM experiments were realized on a JEOL ARM 200F microscope equipped together with a CEOS aberration corrector for the objective lens and a cold FEG. All the experiments were performed with an 80 kV acceleration voltage.[52]

TEM Structural analyses of MWCNTs and Fe@MWCNTs after Aging in THP-1-Derived Macrophages. Cells were seeded onto 75 cm^2 flasks at 12 $\times$ 10^6 cells per flask in the presence of 5 ng/mL of PMA. After 48 h, cells were washed and fresh supplemented media was added for 24 h. Then, cells were pretreated or not for 30 min with 10 mM of NAC and exposed to 5 μg/mL of MWCNTs or Fe@MWCNTs in the presence or absence of NAC. After 24 h incubation time, cells were washed with PBS and fresh supplemented media was added in order to remove the nonphagocytized nanomaterials. At 3, 24, 48, or 168 h after exposure, cells were scraped and a centrifugation step at 350*g* for 10 min was performed to separate the cells from the media. Cells were suspended in the presence of 200 μL of distilled water in a sonication bath at maximum power for 1 min, to lyse them by osmotic shock. Cell lysate was then centrifuged at 10 000*g* for 5 min. Supernatant was eliminated by pipetting and the pellet containing MWCNTs and cell residues was dispersed in water. After a final heating step at 80 °C for 15 min to remove the last cell residues, 10 μL of the suspensions were deposited on carbon TEM grid and then dried for 5 min before TEM and HRTEM observations. To confirm that this extraction procedure did not affect the structure of the MWCNTs, a control sample was realized on 3 mL of suspension used to expose the cells. To compare MWCNTs extracted from cells and MWCNTs from control, both heating (37 °C for 3 to 168 h aging time; 80 °C for 15 min) and centrifugation steps (350*g* for 5 min and 10 000*g* for 5 min) were performed on the suspension in absence of cells. TEM analysis of this control sample revealed that the structure of MWCNTs is not disturbed by the extraction procedure.

Liquid-Cell Sample Preparation. The liquid cells commercialized by Protochips, Inc. consist of two silicon wafers with dimensions of 2 $\times$ 2 mm^2 and 4.5 $\times$ 6 mm^2, called the small and large E-chips, respectively (Figure S9). Each E-chip has one 550 μm $\times$ 50 μm window covered by a 30 nm thick silicon–nitrite amorphous film. A 2.5 μL drop of MWCNT or Fe@MWCNT suspension dispersed in water or in ethanol was deposited on the electron transparent membrane of the small E-chip. The large E-chip was then placed over the small one with their windows in cross-configuration, giving a square field of view of 50 μm edge length. Therefore, the drop of solution was squeezed in between the two E-chips in a volume defined by the thickness of the gold spacers on the small E-chip (150 nm in our case). The entire chamber was then closed by the lid of the holder tip resulting in a vacuum sealed liquid-cell. As illustrated in Figure S9, the impermeability of the liquid cell is ensured by two concentric O-rings. We did not use the holder in flow mode. The thickness of the spacers corresponds to the smallest liquid thickness crossed by the electron beam during the TEM experiment. Indeed, due to the outward bowing of the SiN membranes under vacuum, the smallest liquid thickness is found at the corners of the viewing window. All the images were recorded close to the corners for improving signal-to-noise ratio.

In Situ STEM Imaging. STEM HAADF imaging was performed without changing probe size (5C) and condenser aperture (70 μm) in order to maintain a constant beam current (i_e). The latter was measured on the phosphorescent screen of the microscope prior to insertion of the sample to determine the dose rate focalized on the liquid cell ($i_e = 3.74 \times 10^8$ electron/s or 59.8 pA). MWCNT degradation was followed by continuously recording 512 $\times$ 512 images with a pixel dwell time of 5 μs. In electron microscopy, the dose rate ($\dot{d}$) is usually calculated in electrons/($Å^2 \cdot s$) by dividing i_e by the surface irradiated by the beam, which in STEM mode advantageously corresponds to the imaged area. Therefore, $\dot{d}$ was easily controlled since it is inversely proportional to the square of the magnification. With such optical conditions, $\dot{d}$ varies from 4.5 to 32 electrons/($Å^2 \cdot s$), with the magnification used for imaging (from 150 to 400K). The conversion of $\dot{d}$ in $Gy \cdot s^{-1}$ (*i.e.*, $J \cdot kg^{-1} \cdot s^{-1}$), units commonly used in the field of radiation chemistry, simply requires multiplying $\dot{d}$ in electron/($m^2 \cdot s$) by the density normalized stopping power of the solvent (4.761×10^5 and 4.961×10^5 $eV \cdot m^2/kg$ per electron, at 80 kV for water and ethanol, respectively) and by 1.6×10^{-19} to convert electron-volts to joules. This leads to $\dot{d}$ in between 3.4 $\times$ 10^7 and 2.4 $\times$ 10^8 $Gy \cdot s^{-1}$ for magnification ranging from 150 to 400K in water. $\dot{d}$ is slightly more important in ethanol for equivalent optical conditions.

Cytotoxicity of Degradation Products. At 24 h after exposure, MWCNTs or Fe@MWCNTs were extracted from cells (see extraction procedure above), the degraded MWCNTs and Fe@MWCNTs were suspended in 100 μL of distilled water. The concentrations of the dMWCNT and dFe@MWCNT suspensions were then quantified using DO_{273} quantification method[53] against a standard range of MWCNTs or Fe@MWCNTs. Cytotoxicity tests were then performed by Alamar blue assay for different concentrations of dMWCNTs and dFE@MWCNTs following the same procedure as for MWCNTs and Fe@MWCNTs (see procedure above).

***In Vivo* Degradation of MWCNT Assessment.** Three rats were exposed to 100 μg of MWCNTs by intratracheal instillation. Seven

days after the exposure, the animals were anesthetized. The lungs and the lymph nodes were removed, cut in small sections, and fixed with 2.5% glutaraldehyde. After a postfixation with 1% osmium tetroxide, the samples were dehydrated with ethanol and embedded in EPON 812 (TAAB). The ultrathin sections of 90 and 150 nm, respectively, for TEM analyses were obtained by an ultramicrotome (UCT, Leica), mounted on copper grids, stained with uranyl acetate, and examined in a Tecnai G_2 Biotwin (FEI) electron microscope using an accelerating voltage of 100 kV. Several photographs of $MWCNT_{vi}$ detailed structures were taken, analyzed, and compared to control samples.

NOX_2 Complex and Antioxidant Protein Markers by Reverse Transcription Real Time Polymerase Chain Reaction (RT-qPCR). Cells were seeded onto 6-well plates at 2×10^6 cells per well in the presence of 5 ng/mL of PMA. After 48 h, cells were washed and fresh supplemented media was added for 24 h. Then, cells were pretreated or not for 30 min with 10 mM of NAC and exposed to 5 μg/mL of MWCNTs or Fe@MWCNTs in presence or absence of NAC. After 24 h, cells were washed with PBS and total RNA was extracted from 10^6 cells with NucleoSpin RNA II Kit (Macherey Nagel) according to manufacturer's protocol. One microgram of total RNA was reverse transcribed to cDNA with SuperScript Reverse Transcriptase (Invitrogen, Cat no. 18064-014) according to the manufacturer's protocol using Random primer (Promega, Cat no. C1181) and RNasin (Promega, Cat no. N2511). The quantification of mRNA for RPL19 (housekeeping gene, Fwd 5′-TCATCAAAGATGGGCTGATCAT-3′; Rev 5′-CATCGAGCCCGGGAATG-3′); $NOX_{2\alpha}$ (Fwd 5′-GGGCCCTTTACCAGGAATTACT-3′; Rev 5′-GGCACCGAGAGCAGGAGAT-3′); $NOX_{2\beta}$ (Fwd 5′-TGTGTGAATGCCCGAGTCAA-3′; Rev 5′-TACAGGCCTCCTTCAGGGTT-3′); p47phox (Fwd 5′-CCCATCATCCTGCAGACGTA-3′; Rev 5′-GAGCCCGAGGTCTTCTCGTA-3′); p40phox (Fwd 5′-AGCTCACAAGGCGGGAGTT-3′; Rev 5′-TCAGCGTCCCGGTAATTCAG-3′); p67phox (Fwd 5′-GCCCAGACATTCCAAAATCG-3′; Rev 5′-GGCTCATATAGCTTCTGCTTCCA-3′); MPO (Fwd 5′-GCCAAGCTGAATCGTCAGAAC-3′; Rev 5′-TCATGACCTGCTCAAACAATCG-3′); SOD-Cu (Fwd 5′-CAGGGCATCATCAATTTCGA-3′; Rev 5′-TGCTTCCCCACACCTTCAC-3′); SOD-Mn (Fwd 5′-CGCGGCCTACGTGAACA-3′; Rev 5′-CCAACGCCTCCTGGTACTTC-3′); GSTP-1 (Fwd 5′-CGGGCAACTGAAGCCTTTT-3′; Rev 5′-AAGGTCTTGCCTCCCTGGTT-3′); Ferritin L (Fwd 5′-CGAATTGGCCGAGGAGAA-3′; Rev 5′-GCCACGCTGGTTTTGCAT-3′); Ferritin H (Fwd 5′-TGGCTTGGCGGAATTTCTGT-3′; Rev 5′-GCCCGAGGCTTAGCTTTCAT-3′); iNOS (Fwd 5′-CCCCTTCAATGGCTGGTACA-3′; Rev 5′-GCGCTGGACGTCACAGAA-3′) transcripts was performed using SYBR green PCR master Mix (Applied Biosystems, Cat no. 4367659) according to the manufacturer's protocol on 300 ng of cDNA using StepOne plus Mastercycler (Applied Biosystems). Each sample was run in duplicate.

Protein Quantification Performed by Western Blot Analysis. Cells were seeded onto 6-well plates at 2×10^6 cells per well in the presence of 5 ng/mL of PMA. After 48 h, cells were washed and fresh supplemented media was added for 24 h. Then, cells were pretreated or not for 30 min with 10 mM of NAC and exposed to 5 μg/mL of MWCNTs or Fe@MWCNTs in presence or absence of NAC. After 24 h, cells were washed with PBS and proteins were extracted with Nucler/Cytosol fractionation Kit (Biovision) according to manufacturer's protocol. Presence of $NOX_{2\beta}$ and Ferritin H was analyzed on 50 μg of cytosolic protein by SDS-PAGE (4−20% polyacrylamide, Mniprotean TGX, BioRad). Separated proteins were transferred onto nitrocellulose membranes. Blots were saturated for 1 h in TBST (Tris-base, pH 7.4, Tween 20%)−5% BSA and washed in TBST (3×5 min). They were subsequently incubated for 2 h with a rabbit $NOX_{2\beta}$ or Ferritin H antibody (Santa Cruz) diluted at 1:300 in TBST−BSA 3%. After a washing step in TBST (3×5 min), the membranes were reacted with a goat anti-rabbit-HRP antibody (Santa Cruz) diluted at 1:3300 in TBST−BSA 3%. Presence of proteins was visualized with a chemiluminescent system (ECL+ Western blot detection kit, Amersham). Densitometry of each condition was calculated using ImageJ software. To compare the effect of each treatment, a R_d ratio was calculated as follows:

$$R_d = \frac{D_{ex1} \times D_{con2}}{D_{ex2} \times D_{con1}}$$

where D_{ex1} and D_{ex2} are the densities of exposed groups for NOX_{2b} (or FerH) and RPL19, and D_{con1} and D_{con2} are the densities of control groups for NOX_{2b} (or FerH) and RPL19.

Statistics. All data were expressed as mean ± SD (standard deviation). F-test was used to compare the homogeneity of the variances. If homogeneity of variance was verified with a risk α equal to 5%, differences between each group were assessed with a one-way analysis of variance (ANOVA). When all ANOVA tests were positive, groups were subjected to the multiple-comparison Dunnett's test. If the variances were not homogeneous, no significant differences between groups were considered. $^*P < 0.05$ was considered as the statistical significance level. For each aging time point of 3, 24, 48, and 168 h for CNTs in cells in presence or absence of NAC, percentage of perforated area (P_a), the mean surface area of holes ($\bar{S}$), and the density of holes (D) were measured in MWCNTs and Fe@MWCNTs. Hole surface areas at each time point could be assimilated as a distribution and then compared per pair using Kolmogorov−Smirnov test. P-values obtained by Kolmogorov−Smirnov test which are less than 0.05 show significant differences between the two distributions.

Conflict of Interest: The authors declare no competing financial interest.

Supporting Information Available: The Supporting Information is available free of charge on the ACS Publications website at DOI: 10.1021/acsnano.5b03708.

Additional figures (PDF)
Video accelerated 16 times of nanotube degradation in water (corresponding to Figure 3a) (AVI)

Acknowledgment. This work was supported by the CNRS (Centre National de la Recherche Scientifique, Defi Nano program), the ANR (Agence Nationale de la Recherche) and CGI (Commissariat à l'Investissement d'Avenir) through the LabEx SEAM (Science and Engineering for Advanced Materials and devices; ANR 11 LABX 086, ANR 11 IDEX 05 02) and the LabEx Chemistry of Complex Systems (ANR-10-LABX-0026_CSC), by the ANR project DECANO (ANR-2011-CESA-007-01) and by the International Center for Frontier Research in Chemistry (icFRC).

REFERENCES AND NOTES

1. Lanone, S.; Boczkowski, J. Biomedical Applications and Potential Health Risks of Nanomaterials: Molecular Mechanisms. *Curr. Mol. Med.* **2006**, *6*, 651–663.
2. Sechi, G.; Bedognetti, D.; Sgarrella, F.; Van Eperen, L.; Marincola, F. M.; Bianco, A.; Delogu, L. G. The Perception of Nanotechnology and Nanomedicine: A Worldwide Social Media Study. *Nanomedicine* **2014**, *9*, 1475–1486.
3. Elgrabli, D.; Floriani, M.; Abella-Gallart, S.; Meunier, L.; Gamez, C.; Delalain, P.; Rogerieux, F.; Boczkowski, J.; Lacroix, G. Biodistribution and Clearance of Instilled Carbon Nanotubes in Rat Lung. *Part. Fibre Toxicol.* **2008**, *5*, 20.
4. McDevitt, M. R.; Chattopadhyay, D.; Kappel, B. J.; Jaggi, J. S.; Schiffman, S. R.; Antczak, C.; Njardarson, J. T.; Brentjens, R.; Scheinberg, D. A. Tumor Targeting with Antibody-Functionalized, Radiolabeled Carbon Nanotubes. *J. Nucl. Med.* **2007**, *48*, 1180–1189.
5. Wang, H.; Wang, J.; Deng, X.; Sun, H.; Shi, Z.; Gu, Z.; Liu, Y.; Zhao, Y. Biodistribution of Carbon Single-Wall Carbon Nanotubes in Mice. *J. Nanosci. Nanotechnol.* **2004**, *4*, 1019–1024.
6. Shvedova, A. A.; Kisin, E. R.; Mercer, R.; Murray, A. R.; Johnson, V. J.; Potapovich, A. I.; Tyurina, Y. Y.; Gorelik, O.; Arepalli, S.; Schwegler-Berry, D.; et al. Unusual Inflammatory and Fibrogenic Pulmonary Responses to Single-Walled Carbon Nanotubes in Mice. *Am. J. Physiol.* **2005**, *289*, L698–L708.
7. Flaviu, T.; Catoi, C.; Mocan, T.; Mocan, L.; Biris, A.; Simon, S.; Nagy, A.; Taulescu, M.; Bulfa, P.; Catoi, A. F. Interaction between Kupffer Cells and Carbon Nanotubes-Transition from Biodistribution and Toxicity to Kupffer Cell Targeted Therapy. *Bull. Univ. Agric. Sci. Vet. Med. Cluj-Napoca, Vet. Med.* **2013**, *70*, 147.

8. Lacerda, L.; Ali-Boucetta, H.; Herrero, M. A.; Pastorin, G.; Bianco, A.; Prato, M.; Kostarelos, K. Tissue Histology and Physiology Following Intravenous Administration of Different Types of Functionalized Multiwalled Carbon Nanotubes. *Nanomedicine* **2008**, *3*, 149–161.
9. Cherukuri, P.; Bachilo, S. M.; Litovsky, S. H.; Weisman, R. B. Near-Infrared Fluorescence Microscopy of Single-Walled Carbon Nanotubes in Phagocytic Cells. *J. Am. Chem. Soc.* **2004**, *126*, 15638–15639.
10. Allen, B. L.; Kichambare, P. D.; Gou, P.; Vlasova, I. I.; Kapralov, A. A.; Konduru, N.; Kagan, V. E.; Star, A. Biodegradation of Single-Walled Carbon Nanotubes through Enzymatic Catalysis. *Nano Lett.* **2008**, *8*, 3899–3903.
11. Kagan, V. E.; Konduru, N. V.; Feng, W.; Allen, B. L.; Conroy, J.; Volkov, Y.; Vlasova, I. I.; Belikova, N. A.; Yanamala, N.; Kapralov, A.; et al. Carbon Nanotubes Degraded by Neutrophil Myeloperoxidase Induce Less Pulmonary Inflammation. *Nat. Nanotechnol.* **2010**, *5*, 354–359.
12. Andon, F. T.; Kapralov, A. A.; Yanamala, N.; Feng, W.; Baygan, A.; Chambers, B. J.; Hultenby, K.; Ye, F.; Toprak, M. S.; Brandner, B. D.; et al. Biodegradation of Single-Walled Carbon Nanotubes by Eosinophil Peroxidase. *Small* **2013**, *9*, 2721–2729.
13. Bhattacharya, K.; El-Sayed, R.; Andón, F. T.; Mukherjee, S. P.; Gregory, J.; Li, H.; Zhao, Y.; Seo, W.; Fornara, A.; Brandner, B.; et al. Lactoperoxidase-Mediated Degradation of Single-Walled Carbon Nanotubes in the Presence of Pulmonary Surfactant. *Carbon* **2015**, *91*, 506–517.
14. Farrera, C.; Bhattacharya, K.; Lazzaretto, B.; Andon, F. T.; Hultenby, K.; Kotchey, G. P.; Star, A.; Fadeel, B. Extracellular Entrapment and Degradation of Single-Walled Carbon Nanotubes. *Nanoscale* **2014**, *6*, 6974–83.
15. Russier, J.; Ménard-Moyon, C.; Venturelli, E.; Gravel, E.; Marcolongo, G.; Meneghetti, M.; Doris, E.; Bianco, A. Oxidative Biodegradation of Single- and Multi-Walled Carbon Nanotubes. *Nanoscale* **2011**, *3*, 893–896.
16. Kagan, V. E.; Kapralov, A. A.; St Croix, C. M.; Watkins, S. C.; Kisin, E. R.; Kotchey, G. P.; Balasubramanian, K.; Vlasova, I. I.; Yu, J.; Kim, K.; et al. Lung Macrophages "Digest" Carbon Nanotubes Using a Superoxide/Peroxynitrite Oxidative Pathway. *ACS Nano* **2014**, *8*, 5610–5621.
17. Liu, X.; Marangon, I.; Melinte, G.; Wilhelm, C.; Ménard-Moyon, C.; Pichon, B. P.; Ersen, O.; Aubertin, K.; Baaziz, W.; Pham-Huu, C.; et al. Design of Covalently Functionalized Carbon Nanotubes Filled with Metal Oxide Nanoparticles for Imaging, Therapy, and Magnetic Manipulation. *ACS Nano* **2014**, *8*, 11290–11304.
18. Kagan, V. E.; Tyurina, Y. Y.; Tyurin, V. A.; Konduru, N. V.; Potapovich, A. I.; Osipov, A. N.; Kisin, E. R.; Schwegler-Berry, D.; Mercer, R.; Castranova, V.; et al. Direct and Indirect Effects of Single Walled Carbon Nanotubes on Raw 264.7 Macrophages: Role of Iron. *Toxicol. Lett.* **2006**, *165*, 88–100.
19. Panasenko, O. M.; Chekanov, A. V.; Arnhold, J.; Sergienko, V. I.; Osipov, A. N.; Vladimirov, Y. A. Generation of Free Radicals During Decomposition of Hydroperoxide in the Presence of Myeloperoxidase or Activated Neutrophils. *Biochemistry* **2005**, *70*, 998–1004.
20. Zhao, Y.; Allen, B. L.; Star, A. Enzymatic Degradation of Multiwalled Carbon Nanotubes. *J. Phys. Chem. A* **2011**, *115*, 9536–9544.
21. de Jonge, N.; Ross, F. M. Electron Microscopy of Specimens in Liquid. *Nat. Nanotechnol.* **2011**, *6*, 695–704.
22. Williamson, M. J.; Tromp, R. M.; Vereecken, P. M.; Hull, R.; Ross, F. M. Dynamic Microscopy of Nanoscale Cluster Growth at the Solid-Liquid Interface. *Nat. Mater.* **2003**, *2*, 532–536.
23. Woehl, T. J.; Jungjohann, K. L.; Evans, J. E.; Arslan, I.; Ristenpart, W. D.; Browning, N. D. Experimental Procedures to Mitigate Electron Beam Induced Artifacts During in Situ Fluid Imaging of Nanomaterials. *Ultramicroscopy* **2013**, *127*, 53–63.
24. Schneider, N. M.; Norton, M. M.; Mendel, B. J.; Grogan, J. M.; Ross, F. M.; Bau, H. H. Electron–Water Interactions and Implications for Liquid Cell Electron Microscopy. *J. Phys. Chem. C* **2014**, *118*, 22373–22382.
25. De Clercq, A.; Dachraoui, W.; Margeat, O.; Pelzer, K.; Henry, C. R.; Giorgio, S. Growth of Pt–Pd Nanoparticles Studied in Situ by HRTEM in a Liquid Cell. *J. Phys. Chem. Lett.* **2014**, *5*, 2126–2130.
26. Evans, J. E.; Jungjohann, K. L.; Browning, N. D.; Arslan, I. Controlled Growth of Nanoparticles from Solution with in Situ Liquid Transmission Electron Microscopy. *Nano Lett.* **2011**, *11*, 2809–2813.
27. Zheng, H.; Smith, R. K.; Jun, Y. W.; Kisielowski, C.; Dahmen, U.; Alivisatos, A. P. Observation of Single Colloidal Platinum Nanocrystal Growth Trajectories. *Science* **2009**, *324*, 1309–1312.
28. Alloyeau, D.; Dachraoui, W.; Javed, Y.; Belkahla, H.; Wang, G.; Lecoq, H.; Ammar, S.; Ersen, O.; Wisnet, A.; Gazeau, F.; et al. Unravelling Kinetic and Thermodynamic Effects on the Growth of Gold Nanoplates by Liquid Transmission Electron Microscopy. *Nano Lett.* **2015**, *15*, 2574–2581.
29. Liao, H. G.; Niu, K.; Zheng, H. Observation of Growth of Metal Nanoparticles. *Chem. Commun. (Cambridge, U. K.)* **2013**, *49*, 11720–11727.
30. Zhao, Y.; Burkert, S. C.; Tang, Y.; Sorescu, D. C.; Kapralov, A. A.; Shurin, G. V.; Shurin, M. R.; Kagan, V. E.; Star, A. Nano-Gold Corking and Enzymatic Uncorking of Carbon Nanotube Cups. *J. Am. Chem. Soc.* **2015**, *137*, 675–684.
31. Gardes-Albert, M.; Bonnefont-Rousselot, D.; Abedinzadeh, Z.; Jore, D. Reactive Oxygen Species. How Oxygen May Become Toxic? *Actual. Chim.* **2003**, *11*, 91–96.
32. Li, W.; Bai, Y.; Zhang, Y.; Sun, M.; Cheng, R.; Xu, X.; Chen, Y.; Mo, Y. Effect of Hydroxyl Radical on the Structure of Multi-Walled Carbon Nanotubes. *Synth. Met.* **2005**, *155*, 509–515.
33. Amiri, A.; Memarpoor-Yazdi, M.; Shanbedi, M.; Eshghi, H. Influence of Different Amino Acid Groups on the Free Radical Scavenging Capability of Multi Walled Carbon Nanotubes. *J. Biomed. Mater. Res., Part A* **2013**, *101A*, 2219–2228.
34. Shieh, Y.-T.; Wang, W.-W. Radical Scavenging Efficiencies of Modified and Microwave-Treated Multiwalled Carbon Nanotubes. *Carbon* **2014**, *79*, 354–362.
35. Shukla, P. K.; Mishra, P. C. Effects of Diameter, Length, Chirality and Defects on the Scavenging Action of Single-Walled Carbon Nanotubes for $OH^{\bullet}$ Radicals: A Quantum Computational Study. *Chem. Phys.* **2010**, *369*, 101–107.
36. Dupre-Crochet, S.; Erard, M.; Nubetae, O. Ros Production in Phagocytes: Why, When, and Where? *J. Leukocyte Biol.* **2013**, *94*, 657–670.
37. Guichard, C.; Pedruzzi, E.; Fay, M.; Ben Mkaddem, S.; Coant, N.; Daniel, F.; Ogier-Denis, E. The Nox/Duox Family of ROS-Generating NADPH Oxidases. *Med. Sci. (Paris)* **2006**, *22*, 953–959.
38. Pacher, P.; Beckman, J. S.; Liaudet, L. Nitric Oxide and Peroxynitrite in Health and Disease. *Physiol. Rev.* **2007**, *87*, 315–424.
39. Szabo, C.; Ischiropoulos, H.; Radi, R. Peroxynitrite: Biochemistry, Pathophysiology and Development of Therapeutics. *Nat. Rev. Drug Discovery* **2007**, *6*, 662–680.
40. Ju, L.; Zhang, G.; Zhang, X.; Jia, Z.; Gao, X.; Jiang, Y.; Yan, C.; Duerksen-Hughes, P. J.; Chen, F. F.; Li, H.; et al. Proteomic Analysis of Cellular Response Induced by Multi-Walled Carbon Nanotubes Exposure in A549 Cells. *PLoS One* **2014**, *9*, e84974.
41. Shen, Z. L.; Nie, H. Y.; Wang, H. F.; Yang, B.; Zhong, L. J.; Zou, X. J.; Lou, Y. X.; Liu, D.; Guo, J.; Jia, G. Two Types of MWCNTS with Different Surface Modifications Induce Differential Expression of Proteins in Raw264.7 Cells. *Beijing Daxue Xuebao, Yixueban* **2010**, *42*, 345–350.
42. Witzmann, F. A.; Monteiro-Riviere, N. A. Multi-Walled Carbon Nanotube Exposure Alters Protein Expression in Human Keratinocytes. *Nanomedicine* **2006**, *2*, 158–68.
43. Haniu, H.; Matsuda, Y.; Takeuchi, K.; Kim, Y. A.; Hayashi, T.; Endo, M. Proteomics-Based Safety Evaluation of Multi-Walled Carbon Nanotubes. *Toxicol. Appl. Pharmacol.* **2010**, *242*, 256–262.
44. Montezano, A. C.; Touyz, R. M. Mechanosensitive Regulation of Cortactin by P47phox: A New Paradigm in Cytoskeletal Remodeling. *Circ. Res.* **2013**, *112*, 1522–1525.

45. Shvedova, A. A.; Kisin, E. R.; Murray, A. R.; Kommineni, C.; Castranova, V.; Fadeel, B.; Kagan, V. E. Increased Accumulation of Neutrophils and Decreased Fibrosis in the Lung of NADPH Oxidase-Deficient C57BL/6 Mice Exposed to Carbon Nanotubes. *Toxicol. Appl. Pharmacol.* **2008**, *231*, 235–40.
46. Elgrabli, D.; Abella-Gallart, S.; Robidel, F.; Rogerieux, F.; Boczkowski, J.; Lacroix, G. Induction of Apoptosis and Absence of Inflammation in Rat Lung after Intratracheal Instillation of Multiwalled Carbon Nanotubes. *Toxicology* **2008**, *253*, 131–136.
47. Li, J. G.; Li, W.-X.; Xu, J.-Y.; Cai, X.-Q.; Liu, R.-L.; Li, Y.-J.; Zhao, Q.-F.; Li, Q.-N. Comparative Study of Pathological Lesions Induced by Multiwalled Carbon Nanotubes in Lungs of Mice by Intratracheal Instillation and Inhalation. *Environ. Toxicol.* **2007**, *22*, 415–421.
48. Mitchell, L. A.; Gao, J.; Vander Wal, R.; Gigliotti, A.; Burchiel, S. W.; McDonald, J. D. Pulmonary and Systemic Immune Response to Inhaled Multiwalled Carbon Nanotubes. *Toxicol. Sci.* **2007**, *100*, 203–214.
49. Shvedova, A. A.; Kisin, E. R.; Murray, A. R.; Gorelik, O.; Arepalli, S.; Castranova, V.; Young, S. H.; Gao, F.; Tyurina, Y. Y.; Oury, T. D.; et al. Vitamin E Deficiency Enhances Pulmonary Inflammatory Response and Oxidative Stress Induced by Single-Walled Carbon Nanotubes in C57BL/6 Mice. *Toxicol. Appl. Pharmacol.* **2007**, *221*, 339–348.
50. Baaziz, W.; Begin-Colin, S.; Pichon, B. P.; Florea, I.; Ersen, O.; Zafeiratos, S.; Barbosa, R.; Begin, D.; Pham-Huu, C. High-Density Monodispersed Cobalt Nanoparticles Filled into Multiwalled Carbon Nanotubes. *Chem. Mater.* **2012**, *24*, 1549–1551.
51. Baaziz, W.; Liu, X.; Florea, I.; Begin-Colin, S.; Pichon, B. P.; Ulhaq, C.; Ersen, O.; Soria-Sanchez, M.; Zafeiratos, S.; Janowska, I.; et al. Carbon Nanotube Channels Selectively Filled with Monodispersed $Fe_{3-X}O_4$ Nanoparticles. *J. Mater. Chem. A* **2013**, *1*, 13853–13861.
52. Ricolleau, C.; Nelayah, J.; Oikawa, T.; Kohno, Y.; Braidy, N.; Wang, G.; Hue, F.; Florea, L.; Pierron Bohnes, V.; Alloyeau, D. Performances of an 80−200 Kv Microscope Employing a Cold-FEG and an Aberration-Corrected Objective Lens. *Microscopy (Oxford, U. K.)* **2013**, *62*, 283–293.
53. Attal, S.; Thiruvengadathan, R.; Regev, O. *Anal. Chem.* **2006**, *78*, 8098–8104.